Supporting Information

Stable 15-Ah Anode-Free Li Pouch Cell Enabled by Electron Resonance Effect

Shihao Duan[1‡], Shuoqing Zhang[1,2‡], Xiaoteng Huang[1‡], Haikuo Zhang[1], Ruhong Li[1,3]*, Long Chen[1], Jinze Wang[1], Sheng Dai[4], Guorong Wang[5], Feng Guo[5], Xuezhang Xiao[1], Huilin Pan[4], Lixin Chen[1,6], Tao Deng[2] and Xiulin Fan[1]*

1. State Key Laboratory of Silicon and Advanced Semiconductor Materials, School of Materials Science and Engineering, Zhejiang University, Hangzhou 310058, China

2. China-UK Low Carbon College, Shanghai Jiao Tong University, Shanghai 201306, China

3. ZJU-Hangzhou Global Scientific and Technological Innovation Center, Zhejiang University, Hangzhou 311215, China

4. Department of Chemistry, Zhejiang University, Hangzhou, 310058, China

5. Shanghai Tairui Lithium Battery Technology Co., Ltd., Shanghai, 201600, China

6. Key Laboratory of Hydrogen Storage and Transportation Technology of Zhejiang Province, Hangzhou 310027, China.

‡ These authors contributed equally.

* Correspondence: xlfan@zju.edu.cn

Experimental Section

Chemical reagents. Methoxytrimethylsilane (MOTMS, 99% purity), 1,2,4-trifluorobenzene (124FB, >98% purity), and biphenyl (≥ 99.5% purity) were purchased from Shanghai Aladdin Biochemical Technology Co. 1,2,3-trifluorobenzene (123FB, >98% purity) was purchased from Bide Pharmatech Co., Ltd. Deuterated water (D_2O, 99.9% purity) was purchased from Meryer (Shanghai) Biochemical Technology Co., Ltd. Tetrahydrofuran (THF) was purchased from Sinopharm Chemical Reagent Co. 1,2-diethoxyethane (DEE, ≥99.5%) and diethylene glycol dimethyl ether (G2, ≥99.5%) were purchased from Shanghai Macklin Biochemical Technology Co., Ltd. Battery-grade lithium bis(fluorosulfonyl)imide (LiFSI) and 1,2-dimethoxyethane (DME) were purchased from Dadu New Material Co., Ltd. All purchased solvents were dried with 4 Å molecular sieves (Aladdin) before use.

Electrolyte preparation. Electrolytes were prepared in an Argon-filled glovebox [Mikrouna (Shanghai) Ind. Int. Tech. Co.] with O_2 and H_2O levels below 0.01 ppm. Chemical reagents utilized in this work are listed in *Chemical reagents*.

Electrode preparation and cell assembly. The thick Li (thickness: 450 μm) and thin Li (thickness: 30 μm) foils were purchased from China Energy Lithium Co. For the $LiNi_{0.8}Mn_{0.1}Co_{0.1}O_2$ (NMC811) or $LiCoO_2$ (LCO) electrode, slurries composed of NMC811 (or LCO), polyvinylidene fluoride, carbon black with a weight ratio of 96:2:2 were mixed with a moderate amount NMP as the solvent. Then, the mixed slurries were bladed onto Al foil and drying at 80 °C under vacuum for 12 h. The dried Al foil with NMC811 (or LCO) active materials was punched into discs (diameter: 12 mm) for subsequent cell testing. CR2032 coin cells (Guangdong Canrd New Energy Technology Co.) were assembled for electrochemical measurements, which were kept at 25 °C in a climatic chamber (ShangHai BOLAB Equipment Co., BLC-300). For each coin cell, 120 μL electrolyte was used. Li||Cu and Li||Al cells were assembled by using Li foil (thickness: 450 μm, diameter: 15.6 mm) as anode, Cu foil (diameter: 19 mm, except for those submitted to electrolyte exchange experiments whose was 16 mm) and Al foil (diameter: 21 mm) as cathode, respectively. Symmetrical cells, including Li||Li and stainless steel||stainless steel, were assembled by using two Li foils and steel foils, respectively. Li||NMC811 cells were assembled by using thin Li foil (thickness: 30 μm, diameter:

14 mm) as anode and NMC811 as cathode (capacity: 2.1 mAh cm^{-2}, diameter: 12 mm). Cu||NMC811 coin cells were assembled by using Cu foil (diameter: 19 mm, except for those submitted to quantification tests whose was 14 mm) as anode and NMC811 as cathode (capacity: 2.2 mAh cm^{-2}, diameter: 12 mm). 200 mAh Cu||NMC811 pouch cells were purchased from LIFUN Technology Co., Ltd. and 3.0 g Ah^{-1} electrolyte was added into each pouch cell for testing. A glass fiber membrane (GF-D) was used as the separator for the stainless steel||stainless steel cells, whereas a polyethylene (PE) separator was applied for the other cells.

Galvanostatic charge/discharge tests. Galvanostatic charge/discharge tests of Li||Cu, Li||Li, Li||NMC811, Cu||NMC811 coin cells and 200 mAh Cu||NMC811 pouch cells were performed using the Landt battery test system (Wuhan LAND Electronic Co.). The 15 Ah Cu||NMC811 pouch cell was performed using the NEWARE battery testing system. The Li plating/stripping CE was measured in Li||Cu cells by the modified Aurbach method[1] and cycle method. The processes of modified Aurbach method were as follows: conducting 5 formation cycles by plating 5 mAh cm^{-2} Li on the Cu substrate and stripping to 1 V at 0.5 mA cm^{-2}; plating a 5 mAh cm^{-2} Li reservoir on the Cu substrate; stripping/plating 1 mAh cm^{-2} Li repeatedly for 10 cycles at 0.5 mA cm^{-2}; stripping all the Li deposits to 1 V. The CE was calculated by dividing the total Li stripping capacity by the Li plating capacity except the formation cycle. The cycle method was conducted by plating/stripping 1 mAh cm^{-2} Li repeatedly at 0.5 mA cm^{-2} with a charge cut-off voltage of 1 V. For SEI structural stability test, Li||Cu cells were cycled by plating Li at 0.5 mA cm^{-2} for 2/4/6/8/2 hours for 5 cycles respectively and then stripped to a charge cut-off voltage of 1 V. For full cells, including Li metal cells and anode-free cells, galvanostatic cycling tests were conducted within a voltage window of 2.8-4.4 V (for NMC811 cells) or 2.8-4.5 V (for LCO cells) at 0.2 C charge and 0.5 C discharge. The cycling performance of Li||Li cells was demonstrated by plating/stripping 1 mAh cm^{-2} at a current density of 0.5 mA cm^{-2}.

Li consumption rate test. Preconditioning Li||Cu CR2032 coin cells was carried out by plating 1.2 mAh cm^{-2} of Li onto the Cu foils at a current density of 0.5 mA cm^{-2} and then stripping it at a current density of 0.5 mA cm^{-2} until a voltage cutoff of 1.0 V. A reservoir comprising 4.8 mAh cm^{-2} (Q_T) of Li then was plated onto the Cu foils at a current density of 0.5 mA cm^{-2}, after which 1.2 mAh cm^{-2} (Q_C) was reversibly stripped (3.0 mA cm^{-2}) and

plated (1.0 mA cm^{-2}) for n cycles until a voltage cutoff of 0.5 V. Li loss rates (*LLR*s) were calculated according to the equation below[2]:

$$LLR = \frac{Q_T - Q_C}{n} \#(1)$$

Area specific resistance (ASR) calculations. The *ASR* was calculated each cycle using the following relation:

$$ASR = \frac{\left(\frac{E_{charge}}{Q_{charge}} - \frac{E_{discharge}}{Q_{discharge}}\right) \times A}{I_{charge} + I_{discharge}} \#(2)$$

where E_{charge} is the charge energy, $E_{\text{discharge}}$ is the discharge energy, Q_{charge} is the charge capacity, $Q_{\text{discharge}}$ is the discharge capacity, A is the cathode surface area, I_{charge} is the charge current, and $I_{\text{discharge}}$ is the discharge current[2].

Electrolyte exchange experiments. The electrolyte exchange experiments were conducted by cycling Li||Cu coin cells in 124-LHCE, 123-LHCE and D-S-HCE first, respectively, plating/stripping 1 mAh cm^{-2} Li repeatedly at 0.5 mA cm^{-2} with a charge cut-off voltage of 1 V for 20 cycles, after which the cells were dissembled and the Cu foil with formed SEI and inactive Li were taken out. The acquired Cu substrates were then assembled into new Li||Cu cells with 6.0 M LiFSI/DME electrolyte and cycled using the same protocol.

Galvanic corrosion tests. Li||NMC811 and Cu||NMC811 coin cells were cycled at 0.2 C charge and 0.5 C discharge (1 C = 200 mA g^{-1}) within a voltage window of 2.8-4.4 V for 10 cycles. Afterwards, the cells were rested for 10 days, when electrochemical impedance spectroscopy (EIS) measurements were conducted every 24 hours since the end of the second day.

Electrochemical characterizations. All the cells for electrochemical characterizations were kept at 25 °C in the climatic chamber (ShangHai BOLAB Equipment Co., BLC-300). Electrochemical characterizations were tested on a CHI660E workstation. Linear sweep voltammetry (LSV) was performed on Li||Al cells from 2.5 V to 6.0 V, using scan rates of 0.5 mV s^{-1} at 25 °C. The EIS plots of Li||Li, Li||NMC811 and Cu||NMC811 cells were conducted in the frequency region of 100,000-0.01 Hz with an amplitude of 5 mV. The

values of exchange current density were calculated using the Tafel equation: $\eta = a + b\log(I)$, where η and I are the potential and current, respectively, and a and b are the constant that could be acquired after fitting the data. The activation energy of Li^+ desolvation (E_a) could be calculated according to the Arrhenius equation: $\ln(1/R_{ct}) = \ln A - E_a/RT$, where R_{ct} is the charge-transfer resistance of the Li||Cu coin cells at different temperatures, A is the pre-exponential factor, E_a is the activation energy, R is the ideal gas constant, and T is the temperature.

Characterizations. The nuclear magnetic resonance (NMR) measurements were conducted by a Brucker AVANCE III HD Ascend™ 400 instrument.The microstructure of Li deposits was observed by scanning electron microscopy (SEM) (Jeol JSM-7610FPlus). X-ray photoelectron spectroscopy (XPS) spectra of NMC811 cathodes and Li deposits were obtained by a ULVAC-PHI PHI VersaProbe 4 with an Al Ka X-ray source of 2400 eV. The NMC811 cathodes were retrieved from 30 μm Li||NMC811 coin cells cycled with the following protocal: The cells were firstly cycled with a 0.1 C/0.1 C charge/discharge rate for 2 formation cycles, followed by 40 cycles with 0.2 C/0.5 C charge/discharge rate, with another 0.1 C/0.1 C charge/discharge rate cycle at the end. The above Li deposits were prepared from Li||Cu cells by plating 4 mAh cm^{-2} Li onto the Cu foil after 10 charge/discharge cycles at 0.5 mA cm^{-2}.

Semi-quantification of inactive Li and LiH accumulation on Cu foils. The quantification of inactive Li and LiH accumulation on anodes from cycled Cu||NMC811 coin cells were conducted using a titration gas chromatography (TGC) method, including the following six main steps. (1) After cycling, the Cu||NMC811 coin cell was disassembled in an Ar-filled glovebox. (2) While still in the glovebox, both the Cu foils and separators on the Cu foil side were harvested without washing and sealed in a container with an inside pressure of 1 atm by a rubber septum which is stable against water. (3) After transferring the sample container out of the glovebox, we injected 1 mL of D_2O into the container to react with the inactive Li completely. (4) A gas-tight syringe was used to transfer 1 mL of the resultant gas from the container into the gas chromatography (GC) system. (5) The amount of H_2 and HD was measured by the GC. The GC measurement was conducted by a FULI GC9790II instrument. All the processes minimize the potential damage and contamination during sample transfer, to obtain reliable results.

Quantification of electrolyte consumption in 200 mAh Cu||NMC811 pouch cells. Extraction-gas & ion chromatography (E-G&IC) method was adopted to quantify the remain amounts of solvents/diluents and Li^+ ions in the cycled 200 mAh Cu||NMC811 pouch cells with 0.6 g of initial electrolytes, respectively.

1. Preparation of the extraction agent

DEE was used as the internal label. G2 was used as the extracting solvent. Extraction agent was made by mixing 4 g of DEE with G2 in a 200 mL beaker. Afterwards, the extraction agent is sealed and stored in aluminium bottles for later usage.

2. Extraction of electrolytes in 200 mAh anode-free pouch cells

Inside an argon-filled glovebox (H_2O < 0.1 ppm, O_2 < 0.1 ppm), cut open the gas pocket of a cycled anode-free pouch cell, and inject 1 mL of the extraction agent. The cell was then re-sealed, gently shaken and stored under room temperature. After 7 days, the well-mixed liquid in the cell was extracted and filtered for subsequent measurements.

3. Ion chromatography (IC) and quantification of Li^+

Dilute the extracted liquid of a cycled anode-free pouch cell with deionized H_2O by 200 times. 5 mL of the diluted solution was measured with IC to obtain the concentration of Li^+ in the diluted solution (c_{Li}), which was conducted by a Thermo Scientific ICS-5000+ instrument. The absolute mass of residual Li^+ in the cycled cell m_{Li} could be further calculated through:

$$m_{Li} = c_{Li} \times 200 \times 1.460\ mL\ for\ 124-LHCE\#(3)$$

$$m_{Li} = c_{Li} \times 200 \times 1.455\ mL\ for\ 123-LHCE\#(4)$$

Here, 0.6 g of 124-LHCE and 123-LHCE were measured to have a volume of 0.460 mL and 0.455 mL, respectively.

4. Gas chromatograph (GC) and quantification of DME, MOTMS, 124FB and 123FB

(1) Determination of calibration coefficients

Directly mix 0.6 g of fresh electrolyte into 1 mL of extraction agent. The mixture was further diluted with G2 by 5 times to achieve a standard solution. 1.5 mL of the standard solution was measured with GC (ThermoFisher TRACE1300). The masses of DME, MOTMS, 124FB, 123FB and DEE in the standard solution were known (m_{DME}=44.7 mg, m_{MOTMS}=79.0 mg, m_{124FB}=263.1 mg, m123FB=264.8 mg, m_{DEE}=20.0 mg). The area of peaks attributed to the solvents, diluents and DEE could be collected from the GC result

(S_{DME}, S_{MOTMS}, S_{124FB}, S_{123FB}, S_{DEE}). The calibration coefficients of the solvents and diluents could be calculated through:

$$f_{DME} = \frac{\frac{m_{DME}}{S_{DME}}}{\frac{m_{DEE}}{S_{DEE}}} \#(5)$$

$$f_{MOTMS} = \frac{\frac{m_{MOTMS}}{S_{MOTMS}}}{\frac{m_{DEE}}{S_{DEE}}} \#(6)$$

$$f_{124FB} = \frac{\frac{m_{124FB}}{S_{124FB}}}{\frac{m_{DEE}}{S_{DEE}}} \#(7)$$

$$f_{123FB} = \frac{\frac{m_{123FB}}{S_{123FB}}}{\frac{m_{DEE}}{S_{DEE}}} \#(8)$$

(2) Quantification of the solvents and diluents

Dilute the extracted liquid of a cycled anode-free pouch cell with G2 by 5 times. 1.5 mL of the diluted solution was measured with GC. The area of peaks attributed to DME, MOTMS, 124FB, 123FB and DEE could be collected from the GC result ($S_{DME\text{-}exp}$, $S_{MOTMS\text{-}exp}$, $S_{124FB\text{-}exp}$, $S_{123FB\text{-}exp}$, $S_{DEE\text{-}exp}$). The absolute masses of residual DME ($m_{DME\text{-}exp}$), MOTMS ($m_{MOTMS\text{-}exp}$), 124FB ($m_{124FB\text{-}exp}$), and 123FB ($m_{123FB\text{-}exp}$) in the cycled cells could be calculated through:

$$m_{DME-exp} = m_{DEE} \times f_{DME} \times \frac{S_{DME-exp}}{S_{DEE-exp}} \#(9)$$

$$m_{MOTMS-exp} = m_{DEE} \times f_{MOTMS} \times \frac{S_{MOTMS-exp}}{S_{DEE-exp}} \#(10)$$

$$m_{124FB-exp} = m_{DEE} \times f_{124FB} \times \frac{S_{124FB-exp}}{S_{DEE-exp}} \#(11)$$

$$m_{123FB-exp} = m_{DEE} \times f_{123FB} \times \frac{S_{123FB-exp}}{S_{DEE-exp}} \#(12)$$

Quantification of reversible and irreversible Li. Li||NMC811 and Cu||NMC811 coin cells were cycled for 10, 20, 30, 40 and 50 cycles, after which the cells were dissembled and both the anode foils and separators on the anode side were harvested to compare their reversible active Li residue and irreversible inactive Li accumulation. This process is similar to that in the semi-quantification of inactive Li and LiH as illustrated before. Afterwards, a mixture of biphenyl and THF was used as a chemical metalation reagent to separate the two kinds of Li metal. There is a charge-transfer process between Li and biphenyl followed by Li coordination with ether oxygens in THF. We added 2 mL of biphenyl/THF (with 6.0 wt% of biphenyl) into the air-tight glass bottle containing one anode foil sample obtained in the first step to dissolve the active Li. After a certain period (48 h) at 25 °C, 500 μL of the solution on the top was fetched out and diluted to 10 mL, which was subjected to inductively coupled plasma-optical emission spectrometer (ICP-OES) to determine the amount of dissolved Li by an Agilent 5110(OES) instrument. The undissolved inactive Li was precipitated at the bottom and not taken in the process. The acquired Li^+ concentration could then be converted to the active Li residue mass.

After part of the solution was taken out for active Li quantification, the remaining solution, which contained undissolved inactive Li capsulated by SEI, were used for inactive quantification. Similar to the semi-quantification of inactive Li and LiH, 1 mL of D_2O was injected into the container to react with the inactive Li completely. The generated gas was quickly sampled and transferred for GC measurement. To convert the integrated intensity of D_2 into the mass of inactive Li, a calibration curve was established using pure Li foil with known weight beforehand. The absolute mass of inactive Li was then calculated based on the fitted calibration curve.

Supplementary Note 1:

To extend the electron resonance principle to other salts and diluent families, certain desired characteristics of anion/diluent molecule structures could be speculated from the screening process and electrostatic potential maps shown in Fig. 1c and 1d.

First, although all anions are negatively charged as a molecule, certain negative charge centers should exist to act as interaction sites, which requires the anion not to be spatially symmetrical. This asymmetry could be in some way evaluated by calculating the anisotropy of the anion, which should not be zero. For example, anions such as FSI^- and bis(trifluoromethanesulfonyl)imide anion ($TFSI^-$) have anisotropy values calculated as 19.37 and 26.71, respectively, corresponding to their spatial asymmetrical structures and possible candidates for electron resonance principle. However, the anisotropy values of anions such as PF_6^- and BF_4^- are calculated to be 0 due to their spatial symmetry, which indicates the electron resonance effect is not extendable to these salts.

Second, to acquire the partial charge transfer from anions, certain special electron structures are expected in the diluent molecule. A typical functional group that can interact with anions is the aromatic group due to the electron-deficient π delocalization when an electron-drawing group is connected to the benzene ring. Anion-π interaction has been widely reported in various fields[3-8]. It is reasonable to speculate that similar interaction would occur between selected anions and diluents. However, types and locations of substituent groups connected to the benzene ring could also greatly affect the eventual electron resonance effect. Herein, it is perceived that the aromatic diluent molecule should remain a minimum polarity, but not a zero polarity since it would be difficult to mix with the polar solvents, and avoid an excessive polarity. Take 124FB and 123FB as example, the relatively evenly distributed F substituent atoms enable the π delocalization to remain as a plane above the benzene ring while demonstrating electron deficiency. Therefore, the whole ring plane could interact with the anion (Fig.1d), presenting a stronger electron resonance effect. However, due to the three F atoms being all on one side of the ring, only the other side of 123FB is electron-deficient and could interact with the anion, significantly weakening the possible charge transfer between anion and diluent.

Supplementary Note 2:

Herein, DME was chosen as a solvent due to its cathodic stability to Li metal anode (LMA) and the wide range of adjustable Li^+ concentration within DME, while MOTMS was chosen as another solvent due to its reinforced Si-O bond and anodic stability to high-electron resonance accordingly.

Supplementary Note 3:

Quantification methods, including TGC and E-G&IC, are utilized in this work to investigate the inactive Li accumulation and electrolyte consumption. Possible artifacts associated with these methods are discussed below:

1. TGC

This semi-quantitative TGC approach relies on the established linear correlation between gas signal intensity and relative Li/LiH abundance[9, 10]. Parallel experiments (n = 3–5) yielded RSD <6% for D_2 signals and <9% for HD signals, consistent with the method's inherent repeatability[11]. Cu foils were segmented (central/edge regions) to account for potential spatial inhomogeneity, with signal averaging—consistent with literature showing uniform Li deposition under similar conditions[12]. Artifacts (contamination, SEI reactivity, gas leakage) were excluded *via* glovebox handling, D_2O's selective reactivity, and He purging—validated in prior TGC studies[13]. The method's robustness is further supported by its reproducibility across diverse battery systems, confirming our results are representative of relative Li/LiH content[14].

2. E-G&IC

E-G&IC was performed following validated protocols, relying on the method's established linear calibration (R^2 > 0.997 for organic solvents, R^2 > 0.999 for LiFSI) and low experimental uncertainty (RSD < 4% for replicate samples)[10, 15]. Cells were equilibrated with extraction agent (diglyme + DEE) for 7 days to ensure uniform analyte dissolution, minimizing spatial inhomogeneity effects[12, 15]. Artifacts (contamination, SEI reactivity, peak interference) were excluded *via* literature-validated controls: extraction agent stability toward electrodes/SEI, blank experiment verification, and GC/IC peak resolution[9, 11, 15]. The method's robustness is further supported by cross-validation with ICP-OES, confirming representative quantification of electrolyte components[15].

Supplementary Note 4:

Anode-free Cu||NMC811 cells are sensitive to protocol variations, but the relative advantage of 124-LHCE over control electrolytes is expected to persist under relaxed conditions, supported by literature and electrolyte fundamentals:

Reduced upper cut-off voltage (4.2–4.3 V): LHCEs exhibit stable solvation structures across 3.0–4.5 V, minimizing electrolyte decomposition even at 4.2–4.3 V. Xiao et al. reported LHCEs retain >99% CE at 4.2 V, outperforming carbonate-based electrolytes by 1–2% due to suppressed electrolyte decomposition—consistent with 124-LHCE's intrinsic CEI stabilization[16].

Lower discharge C-rate (*e.g.*, 0.2 C): At low discharge current densities (≈0.8 mA cm^{-2}), 124-LHCE's LiF-rich SEI ensures compact Li deposition, avoiding the porous morphology that plagues controls. Fang et al. showed Li morphology remains uniform for LHCEs at 0.2 mA cm^{-2}, while controls form dendritic deposits—confirming 124-LHCE's advantage persists at relaxed discharge rates[17].

These observations underscore that 124-LHCE's core advantages (stable SEI, compact Li deposition, and suppressed parasitic reactions) are intrinsic to its localized high-concentration structure, ensuring generalizability across practical protocol variations.

Table S1 | Full names, abbreviations, molecular structures and CAS numbers of the investigated diluents in this work.

Full name	Abbreviation	Molecular	CAS number
benzene	Ph	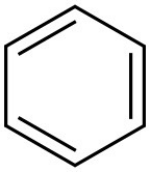	71-43-2
fluorobenzene	FB	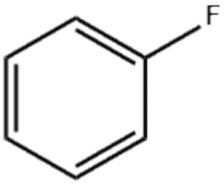	462-06-6
1,2-difluorobenzene	12FB	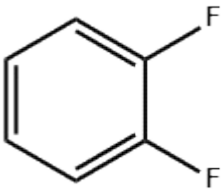	367-11-3
1,3-difluorobenzene	13FB	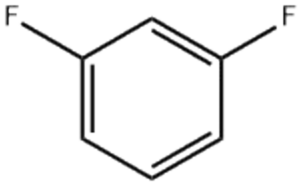	372-18-9
1,4-difluorobenzene	14FB	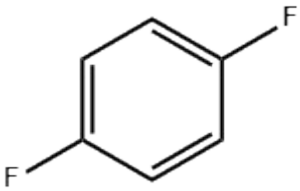	540-36-3
1,2,3-trifluorobenzene	123FB	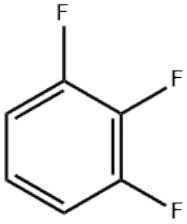	1489-53-8
1,2,4-trifluorobenzene	124FB	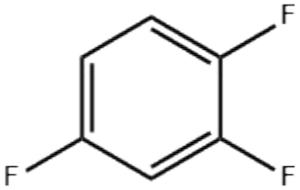	367-23-7

Full name	Abbreviation	Molecular	CAS number
1,3,5-trifluorobenzene	135FB	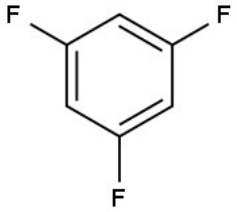	372-38-3
1,2,3,4-tetrafluorobenzene	1234FB	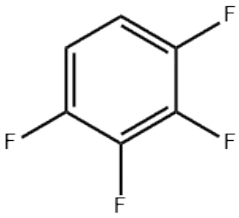	551-62-2
1,2,3,5-tetrafluorobenzene	1235FB	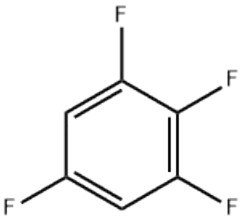	2367-82-0
1,2,4,5-tetrafluorobenzene	1245FB	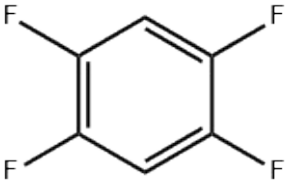	327-54-8
pentafluorobenzene	5FB	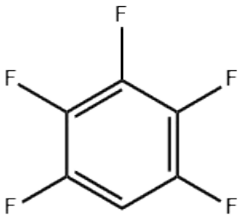	363-72-4
hexafluorobenzene	HFB	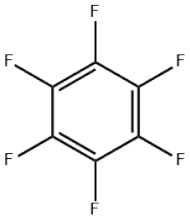	392-56-3
2,2-bis(trifluoromethyl)-1,3-dioxolane	BTFMD	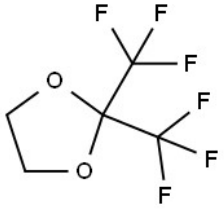	367-23-7

Full name	Abbreviation	Molecular	CAS number
diphenyl ether	DPE	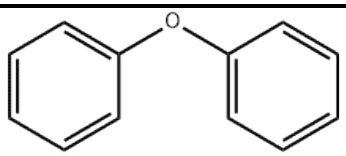	101-84-8
ethyl 1,1,2,2-tetrafluoroethyl ether	ETE	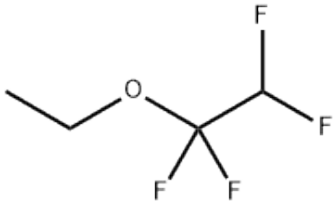	512-51-6
(trifluoromethyl)cyclohexane	FMCH	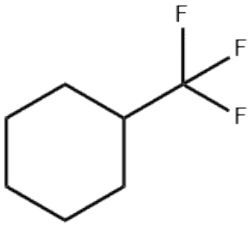	401-75-2
p-fluorotoluene	F-Tol	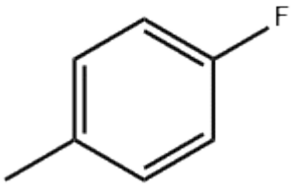	352-32-9
2H,3H-decafluoropentane	HFC	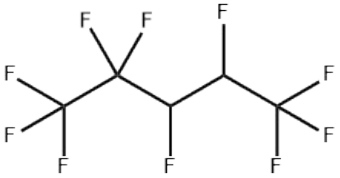	138495-42-8
1,1,2,2,3,3,4-heptafluorocyclopentane	HFCP	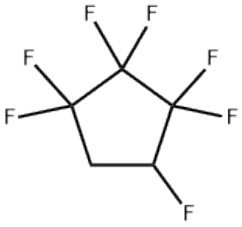	15290-77-4

Full name	Abbreviation	Molecular	CAS number
hexane	Hex		110-54-3
sevoflurane	HFP	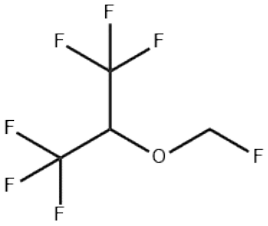	28523-86-6
2H-pyran, 3,3,4,4,5,5-hexafluorotetrahydro-	HFTHP	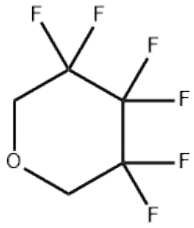	355-09-9
n-butyl methyl ether	MNBE		628-28-4
1H,1H,5H-perfluoropentyl-1,1,2,2-tetrafluoroethylether	OFE	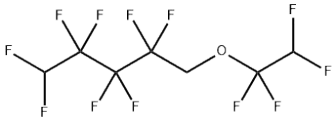	16627-71-7
1,1,2,2-tetrafluoroethyl 2,2,2-trifluoroethyl ether	TFETFE	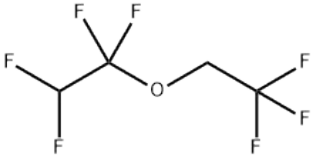	406-78-0
toluene	Tol	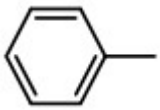	108-88-3

Table S2 | Suppliers and prices of the investigated diluents in this work.

Abbreviation	Supplier	Price (CNY g^{-1})	Price (USD g^{-1})
Ph	Aladdin	0.54	0.08
FB	Aladdin	0.66	0.09
12FB	Aladdin	1.33	0.19
13FB	Aladdin	2.70	0.39
14FB	Aladdin	3.61	0.52
123FB	Aladdin	2.82	0.40
124FB	Aladdin	3.10	0.44
135FB	Aladdin	7.07	1.01
1234FB	Aladdin	12.44	1.77
1235FB	Aladdin	131.92	18.82
1245FB	Aladdin	3.85	0.55
5FB	Aladdin	3.74	0.53
HFB	Aladdin	14.75	2.10
BTFMD	Aladdin	3.10	0.44
DPE	Aladdin	0.17	0.02
ETE	Aladdin	17.40	2.48
FMCH	Aladdin	24.64	3.52
F-Tol	Aladdin	0.93	0.13
HFC	Aladdin	4.96	0.71
HFCP	Aladdin	8.24	1.18
Hex	Aladdin	0.67	0.10
HFP	Aladdin	233.10	33.26
HFTHP	TCI	318.40	45.43
MNBE	Aladdin	21.71	3.10
OFE	Aladdin	6.90	0.98
TFETFE	Aladdin	2.46	0.35
Tol	Vokai	0.37	0.05

Table S3 | Stringency assessment of the adopted galvanostatic protocol.

Protocol parameter	Value in this work	Stringency Rationale
Charge/discharge C-rate	0.2 C charge/0.5 C discharge	Asymmetric moderate-to-high rate
Upper cut-off voltage	4.4 V vs. Li/Li^+	Demanding
Formation cycles	1 cycle (room temperature)	Stringent
Voltage window	2.8–4.4 V	Covers full NMC811 redox range

Table S4 | Summary of the Li inventory parameters of different cell types.

Cell type	Electrolyte	N/P	E/C ($g\ Ah^{-1}$)	Initial Li inventory	Average Li loss rate ($cycle^{-1}$) *
Coin cell	124-LHCE	0	~ 36	0	~ 0.84%
Coin cell	123-LHCE	0	~ 36	0	~ 1.06%
200 mAh Pouch cell	124-LHCE	0	3	0	~ 0.97%
200 mAh Pouch cell	123-LHCE	0	3	0	~ 1.03%
15 Ah Pouch cell	124-LHCE	0	3	0	~ 0.52%

* Average Li loss rate is calculated based on the first 50 cycles for all cell types and formation cycles are excluded.

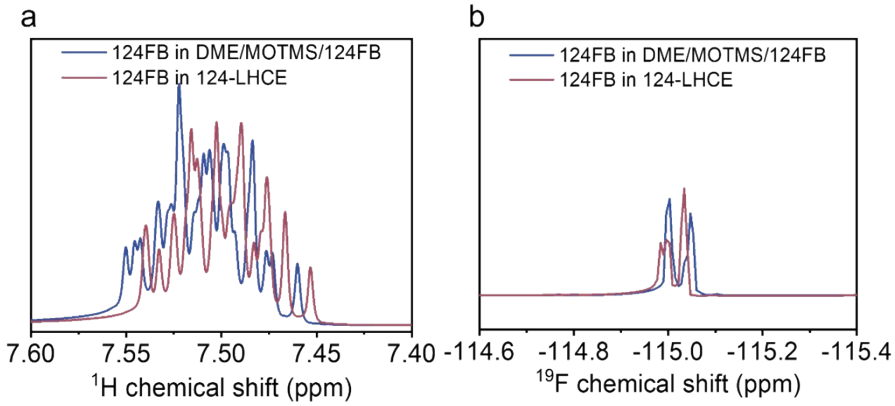

Fig. S1 | (a) ^{1}H and **(b)** ^{19}F NMR spectra of 124-LHCE and DME/MOTMS/124FB mixture with no LiFSI.

The electron resonance interaction between FSI^- anion and 124FB solvent was identified using ^{1}H and ^{19}F NMR signals of solvent mixture with or without salt addition, which show a downfield shift in ^{1}H spectra (Fig. S1a) and an upfield shift in ^{19}F spectra (Fig. S1b) after LiFSI addition. The shift in ^{1}H and ^{19}F NMR spectra of 124FB suggests change of electron densities surrounding the molecules, which results from the electron resonance interaction with the anions.

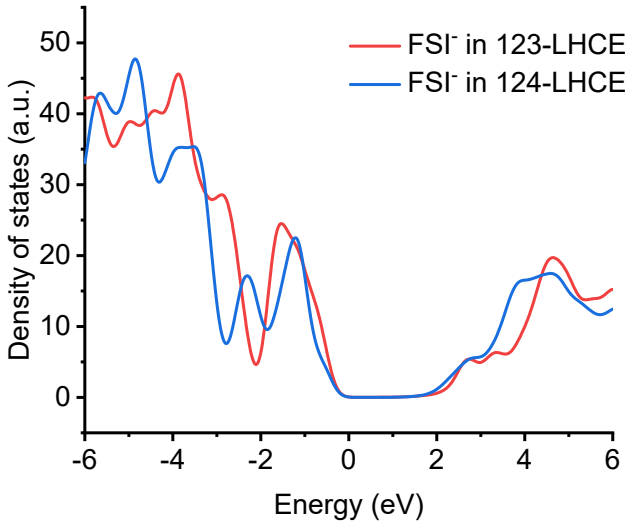

Fig. S2 | Density of states of 123-LHCE and 124-LHCE.

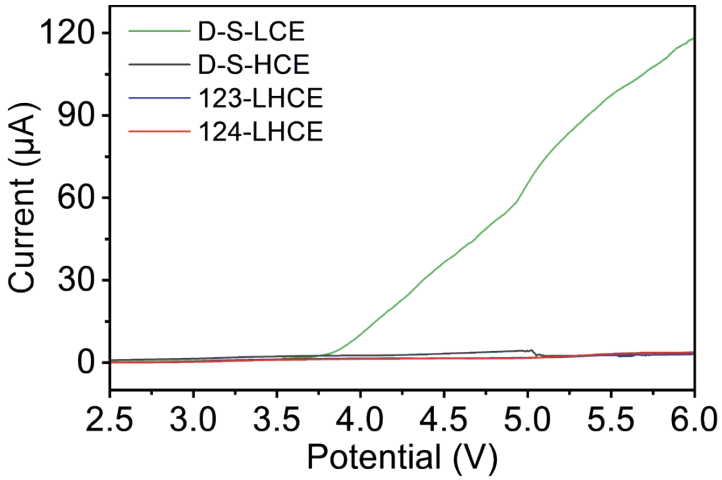

Fig. S3 | LSV tests of D-S-HCE, 123-LHCE and 124-LHCE compared with D-S-LCE.

As shown in Fig. S3, all high concentration and localized high concentration electrolytes, including D-S-HCE, 123-LHCE and 124-LHCE, remained stable up to 6 V. However, a relatively low concentration electrolyte, *i.e.*, 2.2 M LiFSI in DME/MOTMS (1:2 by volume, abbreviated as D-S-LCE) started to exhibit significant decomposition at ~3.5 V.

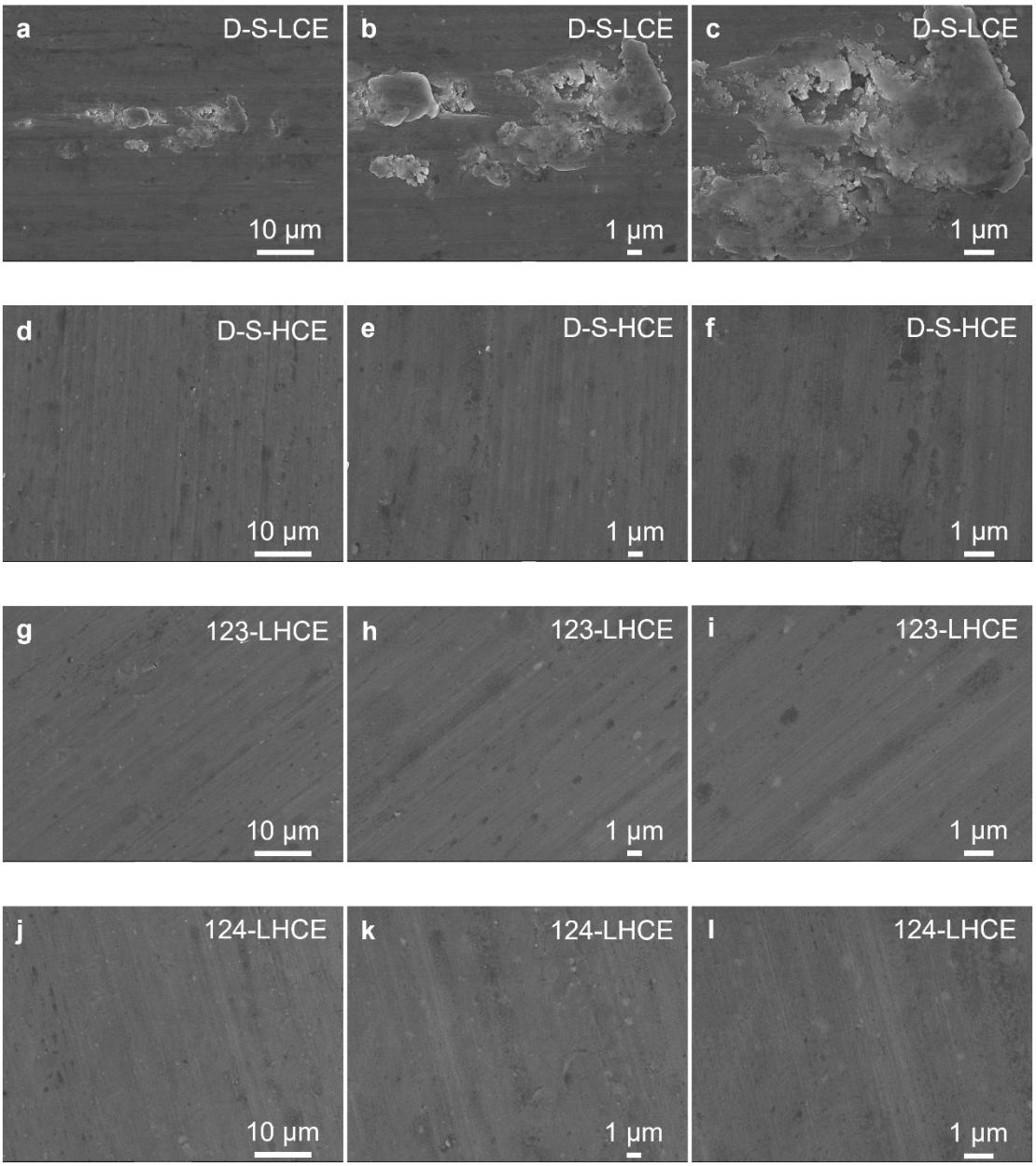

Fig. S4 | SEM images of Al foils corroded at 4.4 V for 24 h by **(a-c)** D-S-LCE, **(d-f)** D-S-HCE, **(g-i)** 123-LHCE and **(j-l)** 124-LHCE, respectively.

Al corrosion tests were carried out to check on the compatibility of electrolytes with cathode-side Al foils. Li||Al cells were assembled and charged to 4.4 V, followed by a 24-hour 4.4-V potentiostatic step. Al foils with D-S-LCE showed obvious corrosion pits after the tests (Fig. S4a-c), while no observable corrosion could be found in foils with D-S-HCE, 123-LHCE and 124-LHCE.

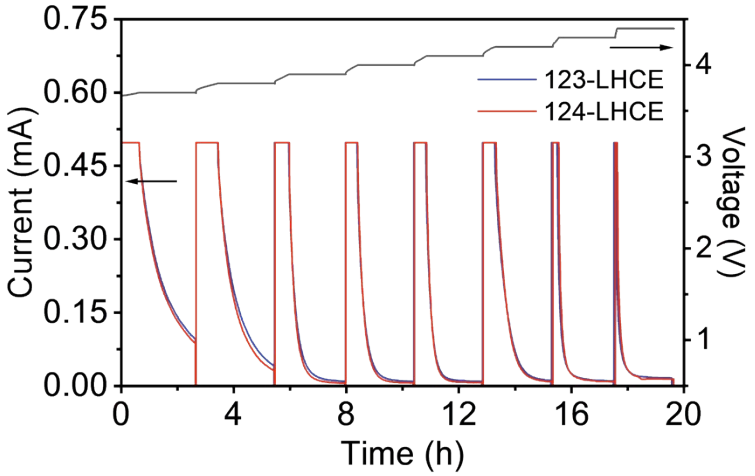

Fig. S5 | Step constant voltage plot of Li||NMC811 full cells paired with 124-LHCE and 123-LHCE, respectively.

Step constant voltage tests were carried out for Li||NMC811 full cells with 124-LHCE and 123-LHCE. The cells were charged at 0.2 C to the upper cut-off voltage, followed by a 2-hour potentiostatic charging step. The upper cut-off voltage was set from 3.7 V to 4.4 V with a 0.1 V step. As shown in Fig. S5, lower leakage currents were observed for the cell with 124-LHCE, especially at initial charging voltages below 4.4 V.

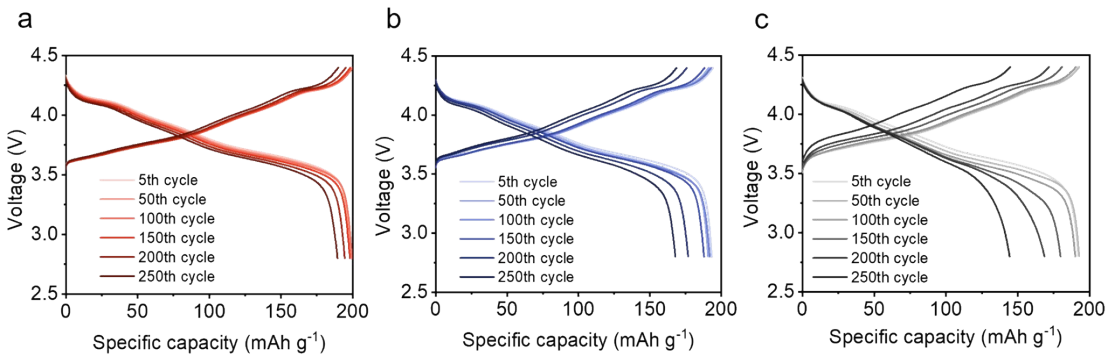

Fig. S6 | Capacity-voltage plots of 30 μm Li||NMC811 coin cells cycled in **(a)** 124-LHCE, **(b)** 123-LHCE and **(c)** D-S-HCE.

The stable overpotentials throughout the long cycling indicate the stable electrode/electrolyte interphases in 124-LHCE (Fig. S6a), while the resistive interphases in 123-LHCE and D-S-HCE continuously enlarge the voltage hysteresis (Fig. S6b and c).

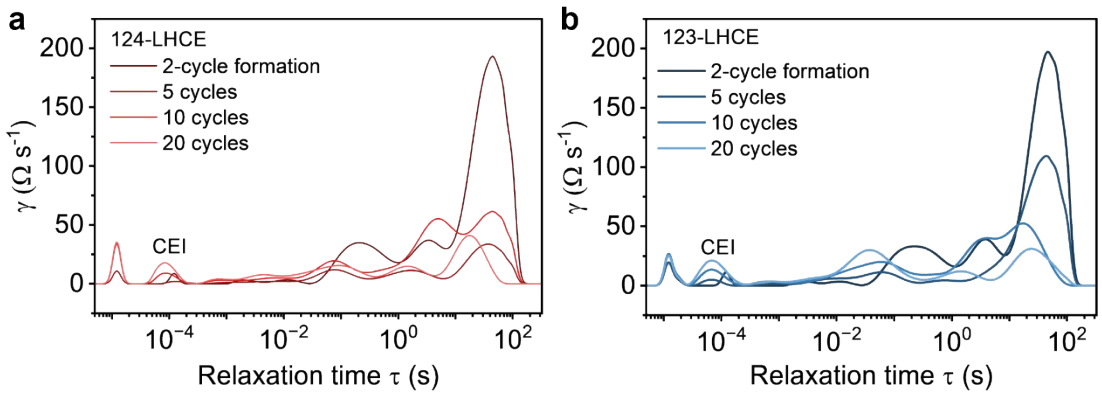

Fig. S7 | Cycle-number-dependent distribution of relaxation times plot derived from EIS data for 124-LHCE and 123-LHCE in Li||NMC811 cells.

EIS and resistance relaxation analyses were conducted. As shown in Fig. S7, the 123-LHCE exhibited higher CEI resistance increase during cycling, likely due to the formation of a relatively unstable and resistive CEI. In contrast, 124-LHCE demonstrated lower CEI resistance values across the cycling process, highlighting its superior oxidation resistance. This stable CEI is essential for protecting electrode materials during prolonged cycling[18].

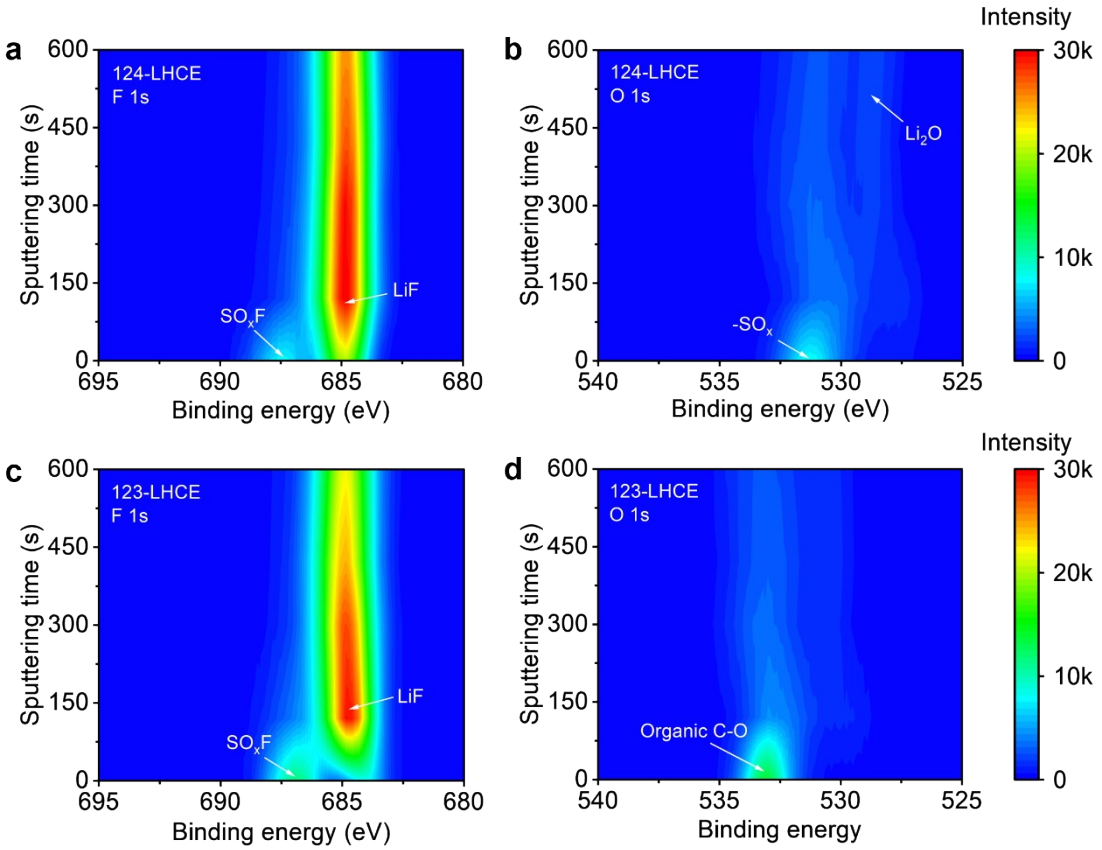

Fig. S8 | XPS depth profiles of **(a, c)** F 1s spectra and **(b, d)** O 1s spectra in CEI produced in 124-LHCE and 123-LHCE retrieved from cycled NMC811 cathodes, respectively.

The CEI formed in 124-LHCE was demonstrated to be more enriched in LiF and Li_2O containing inorganic products, while the CEI formed in 123-LHCE contained more organic components at the surface. The more inorganic-rich CEI in 124-LHCE was consistent with its superior cycling performance when paired with NMC811 cathode.

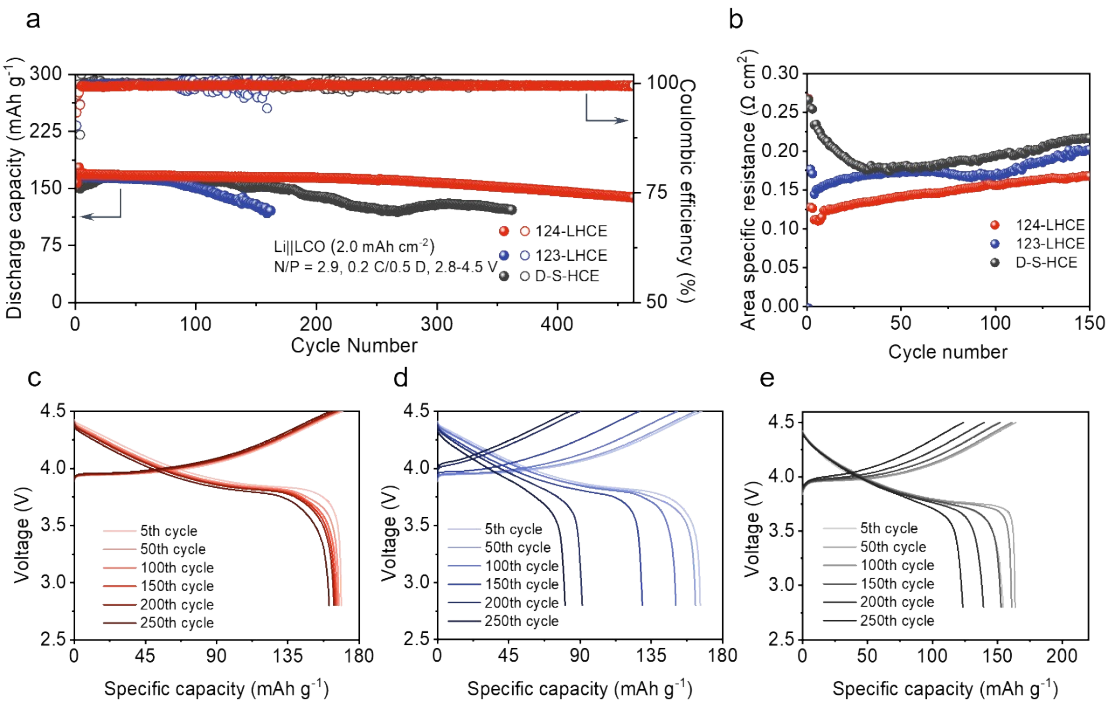

Fig. S9 | Cycle performance of 30 µm Li||LCO coin cells. (a) Discharge capacity profile. **(b)** Area specific resistance evolution calculated from (a). **(c-e)** Capacity-voltage plots of **(c)** 124-LHCE, **(d)** 123-LHCE and **(e)** D-S-HCE.

When cycled at a deep charge/discharge cut-off voltage of 2.8-4.5 V using an LCO cathode, the cell with 123-LHCE could only survive within ~150 cycles, while 123-LHCE lasted for ~350 cycles (Fig. S9a). Under the same condition, the cell using 124-LHCE retained 80% capacity after 486 cycles with much less polarization (Fig. S9c-e). The evolution of area specific resistance was discerned from the charge and discharge curves[2]. 124-LHCE exhibited the slowest rise in area specific resistance, reaching ~0.17 Ω cm^2 after 150 cycles, while both D-S-HCE and 123-LHCE reached above 0.20 Ω cm^2 (Fig. S9b).

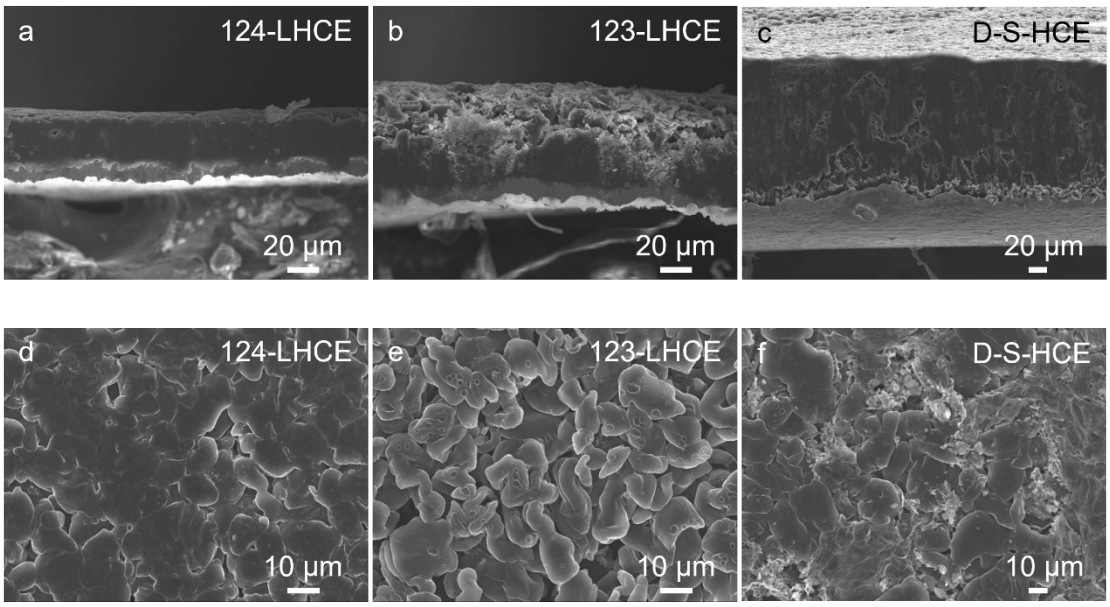

Fig. S10 | SEM of Li deposits in **(a, d)** 124-LHCE, **(b, e)** 123-LHCE and **(c, f)** D-S-HCE. **(a-c)** Top-view and **(d-f)** cross-sectional view SEM images of the deposited Li on Li metal anode.

The micromorphology provides a key insight into the compatibility of LMA and electrolytes. Li deposits with a capacity of 6 mAh cm^{-2} were used for SEM examination. The Li deposits in 124-LHCE (30.61 μm, Fig. S10a) were much thinner than those in 123-LHCE (45.64 μm, Fig. S10b) and D-S-HCE (115.5 μm, Fig. S10c). The chunky Li granules reduce the surface area exposed to electrolyte, suppressing the continuous electrolyte decomposition and undesired dead Li accumulation. Moreover, 124-LHCE realized flat Li deposits and favored dense and bulky Li growth with uniform coverage on the Cu substrate (Fig. S10d). By comparison, 123-LHCE caused significant intergranular voids among Li deposits (Fig. S10e) while D-S-HCE resulted in loose Li grains with a high structural tortuosity (Fig. S10f). This inhomogeneous deposition could easily generate inactive Li and dendritic Li, facilitating Li inventory loss and unexpected short circuits.

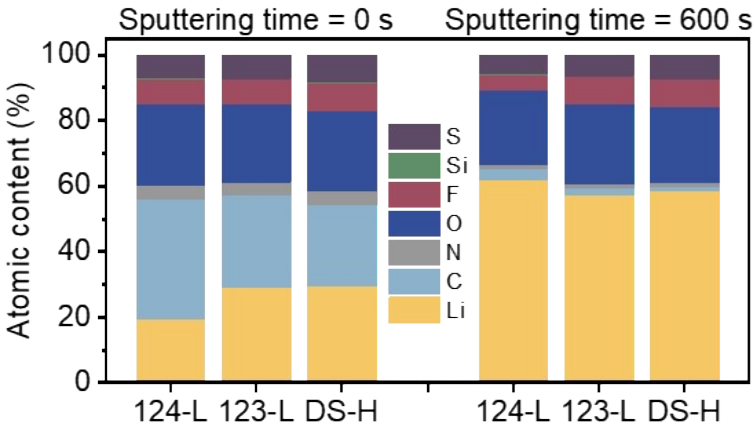

Fig. S11 | Comparison of the SEI atomic make-up of the Li anode extracted from Li||Cu cells after 10 cycles.

The surface layer of Li deposited in 124-LHCE demonstrated largest decrease in the C atomic content and largest increase in the Li atomic content, which indicates organic matrix and inorganic Li compounds respectively, in comparison with 123-LHCE and D-S-HCE.

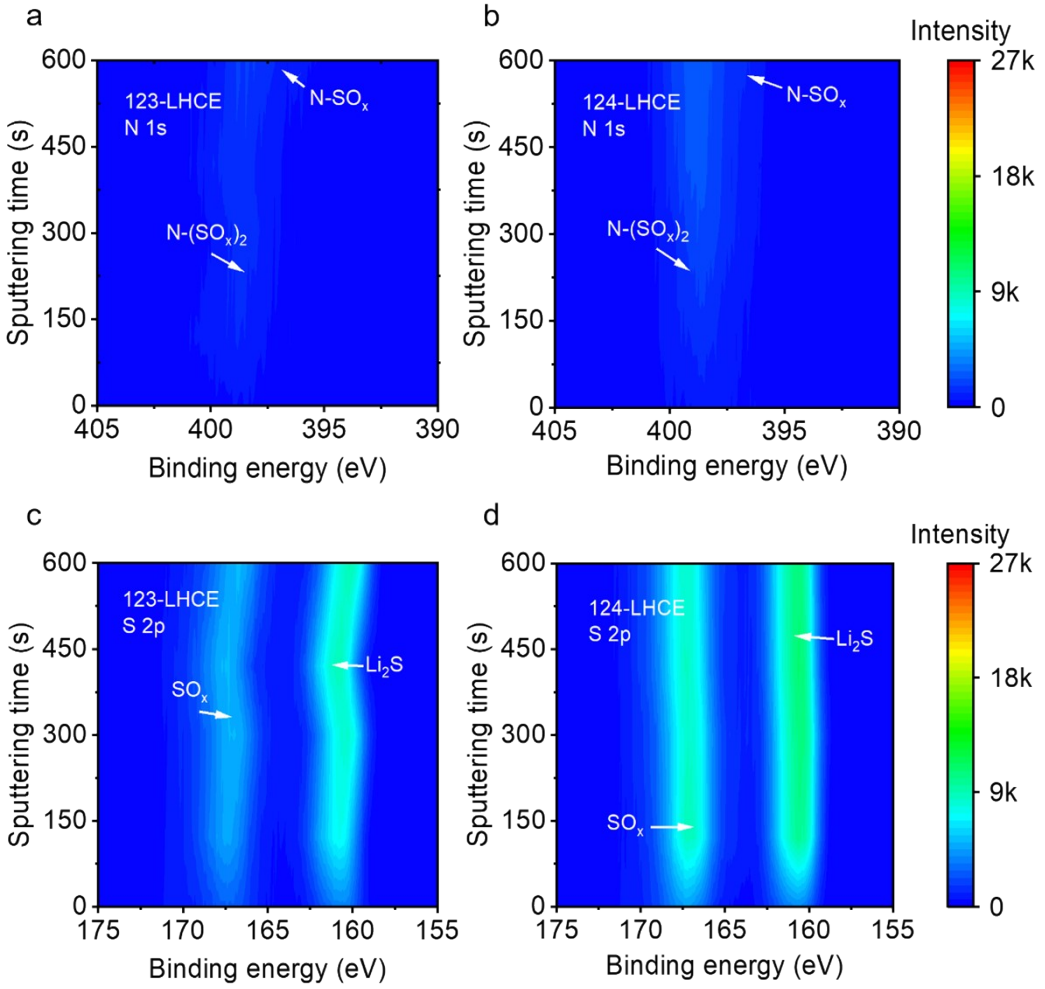

Fig. S12 | XPS depth profiles of **(a, b)** N 1s spectra and **(c, d)** S 2p spectra in 124-LHCE and 123-LHCE, respectively.

The SEI formed in 124-LHCE was demonstrated to be more enriched in N and S containing inorganic products, including N-SO_x, N-$(SO_x)_2$, SO_x and Li_2S, which mainly came from FSI^- anion decomposition.

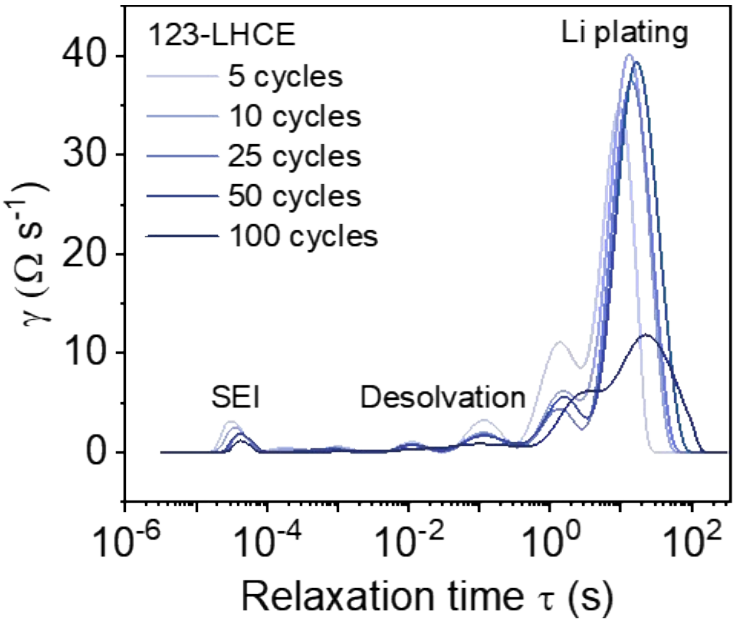

Fig. S13 | Cycle-number-dependent distribution of relaxation times plot derived from EIS data for 123-LHCE in Li||Li symmetric cell.

The Li deposit in 123-LHCE exhibited a Li plating impedance of ~40 Ω s^{-1} during the first 25 cycles, indicating a sluggish Li plating kinetics.

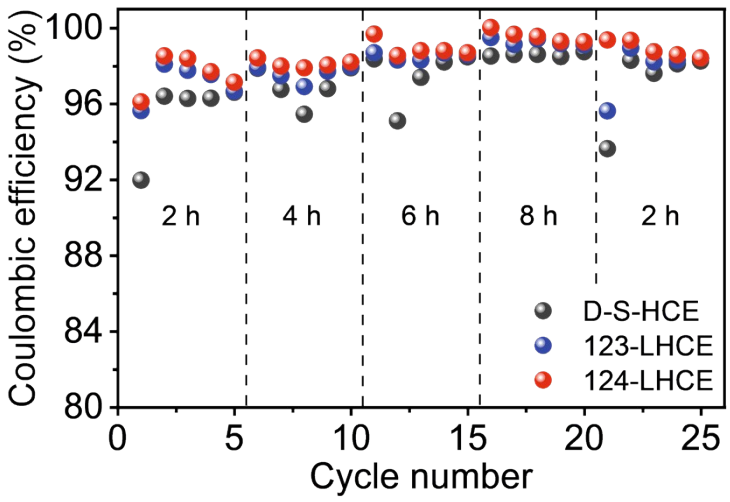

Fig. S14 | CE profiles of the Li||Cu cells cycled in 124-LHCE, 123-LHCE and D-S-HCE with different Li plating time.

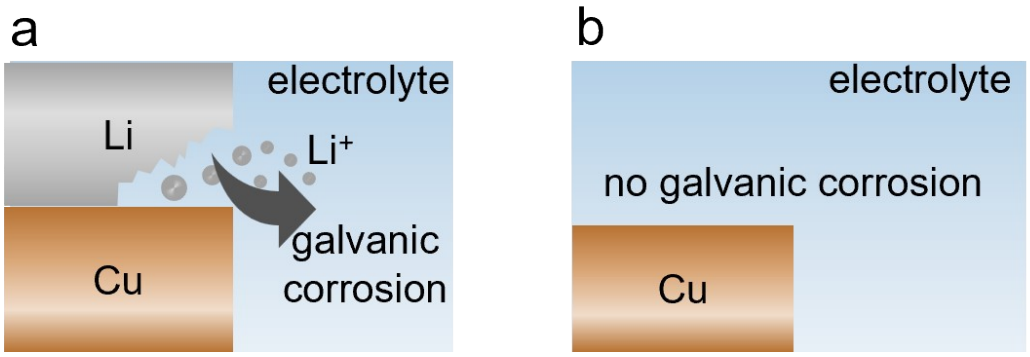

Fig. S15 | Schematic representation showing **(a)** galvanic corrosion on LMA and **(b)** relieved situation on Li-free Cu foil.

Due to the presence of metallic current collectors, galvanic corrosion must be taken into consideration, especially in pouch cells with high capacities where the enlarged electrode area would deteriorate the corrosion. For Li metal batteries, such galvanic corrosion occurs at Cu/Li interfaces with Cu being a substrate for Li, especially when both Li and Cu are emerged in electrolyte[19]. While Cu current collector is stable enough to resist any electrochemical reduction, galvanic corrosion results in oxidation (dissolution) of Li and electrolyte reduction which can result in serious Li inventory loss and electrolyte exhaustion as shown in Fig. S15a. However, such problems could be evaded if no Li is implemented on Cu at all, i.e., in initial anode-free cells, retaining the limited electrolyte resources and enhancing the critical battery safety (Fig. S15b).

References:

1. B. D. Adams, J. Zheng, X. Ren, W. Xu and J.-G. Zhang, *Adv. Energy Mater.*, 2018, **8**, 1702097.
2. Y. Ko, M. A. Baird, X. Peng, T. Ogunfunmi, Y.-W. Byeon, L. M. Klivansky, H. Kim, M. C. Scott, J. Chen, A. J. D'Angelo, J. Chen, S. Sripad, V. Viswanathan and B. A. Helms, *Joule*, 2024, **8**, 814-826.
3. K. Morokuma, *J. Chem. Phys.*, 1971, **55**, 1236-1244.
4. A. Yella, H.-W. Lee, H. N. Tsao, C. Yi, A. K. Chandiran, M. K. Nazeeruddin, E. W.-G. Diau, C.-Y. Yeh, S. M. Zakeeruddin and M. Grätzel, *Science*, 2011, **334**, 629-634.
5. S. Mathew, A. Yella, P. Gao, R. Humphry-Baker, B. F. E. Curchod, N. Ashari-Astani, I. Tavernelli, U. Rothlisberger, M. K. Nazeeruddin and M. Grätzel, *Nature Chemistry*, 2014, **6**, 242-247.
6. T. Zhou, J. Wang, L. Lv, R. Li, L. Chen, S. Zhang, H. Zhang, B. Ma, J. Huang, B. Wu, L. Chen, T. Deng and X. Fan, *Energy & Environmental Science*, 2024, DOI: 10.1039/D4EE03027C.
7. J. Zhou, Y. Luo, R. Li, L. Tian, K. Zhao, J. Shen, D. Jin, Z. Peng, L. Yao, L. Zhang, Q. Liu, S. Zhang, L. Jin, S. Chu, S. Wang, Y. Tian, J. Xu, X. Zhang, P. Shi, X. Wang, W. Fan, X. Sun, J. Sun, L.-Z. Chen, G. Wu, W. Shi, H.-F. Wang, T. Deng, R. Wang, D. Yang and J. Xue, *Nature Chemistry*, 2025, DOI: 10.1038/s41557-025-01732-z.
8. J. Huang, S. Zhang, B. Wan, W. Liu, R. Li, Z. Yang, L. Li, J. Hua, F. Chu, M. Li, T. Zhou, J. Wang, Y. Wu, Z.-R. Li, L. Fan, L. Chen, T. Deng and X. Fan, *Energy & Environmental Science*, 2025, DOI: 10.1039/D5EE05221A.
9. C. Fang, J. Li, M. Zhang, Y. Zhang, F. Yang, J. Z. Lee, M.-H. Lee, J. Alvarado, M. A. Schroeder, Y. Yang, B. Lu, N. Williams, M. Ceja, L. Yang, M. Cai, J. Gu, K. Xu, X. Wang and Y. S. Meng, *Nature*, 2019, **572**, 511-515.
10. W. Bao, C. Fang, D. Cheng, Y. Zhang, B. Lu, D. H. S. Tan, R. Shimizu, B. Sreenarayanan, S. Bai, W. Li, M. Zhang and Y. S. Meng, *Cell Reports Physical Science*, 2021, **2**, 100597.
11. Y. Xiang, M. Tao, G. Zhong, Z. Liang, G. Zheng, X. Huang, X. Liu, Y. Jin, N. Xu, M. Armand, J.-G. Zhang, K. Xu, R. Fu and Y. Yang, *Science Advances*, 2021, **7**, eabj3423.
12. J.-F. Ding, R. Xu, X.-X. Ma, Y. Xiao, Y.-X. Yao, C. Yan and J.-Q. Huang, *Angewandte Chemie International Edition*, 2022, **61**, e202115602.
13. M.-Y. Zhou, X.-Q. Ding, J.-F. Ding, L.-P. Hou, P. Shi, J. Xie, B.-Q. Li, J.-Q. Huang, X.-Q. Zhang and Q. Zhang, *Joule*, 2022, **6**, 2122-2137.
14. G. M. Hobold, C. Wang, K. Steinberg, Y. Li and B. M. Gallant, *Nature Energy*, 2024, **9**, 580-591.
15. H. Wang, X. Yan, R. Zhang, J. Sun, F. Feng, H. Li, J. Liang, Y. Wang, G. Ye, X. Luo, S. Huang, P. Wan, S. T. Hung, F. Ye, F. Chen, E. Wu, J. Zhou, U. Ulissi, X. Ge, C. Liu, B. Xu, N. Liu and C. Ouyang, *Nature Nanotechnology*, 2025, **20**, 1034-1042.
16. J. Xiao, Q. Li, Y. Bi, M. Cai, B. Dunn, T. Glossmann, J. Liu, T. Osaka, R. Sugiura, B. Wu, J. Yang, J.-G. Zhang and M. S. Whittingham, *Nature Energy*, 2020, **5**, 561-568.
17. C. Fang, B. Lu, G. Pawar, M. Zhang, D. Cheng, S. Chen, M. Ceja, J.-M. Doux, H. Musrock, M. Cai, B. Liaw and Y. S. Meng, *Nature Energy*, 2021, **6**, 987-994.
18. S. Jiang, L. Chen, J. Wang, J. Zheng, L. Li, L. Chen, M. Noked, R. Li and X. Fan, *Angewandte Chemie International Edition*, 2025, **64**, e202511863.
19. A. Kolesnikov, M. Kolek, J. F. Dohmann, F. Horsthemke, M. Börner, P. Bieker, M. Winter and M. C. Stan, *Advanced Energy Materials*, 2020, **10**, 2000017.